

Seasonality of submesoscale dynamics in the Kuroshio Extension

Cesar B. Rocha¹, Sarah T. Gille¹, Teresa K. Chereskin¹, and Dimitris Menemenlis²

Key Points.

- Upper-ocean submesoscale (here 10-100 km) turbulence and inertia-gravity waves undergo strong seasonal cycles that are out of phase.
- Submesoscale turbulence dominates the horizontal velocity and sea-surface height variability in late winter/early spring.
- Submesoscale inertia-gravity waves dominate the horizontal velocity and sea-surface height variability in late summer/early fall.

Recent studies show that the vigorous seasonal cycle of the mixed layer modulates upper-ocean submesoscale turbulence. Here we provide model-based evidence that the seasonally-changing upper-ocean stratification in the Kuroshio Extension also modulates submesoscale (here 10-100 km) inertia-gravity waves. Summertime re-stratification weakens submesoscale turbulence but enhances inertia-gravity waves near the surface. Thus, submesoscale turbulence and inertia-gravity waves undergo vigorous out-of-phase seasonal cycles. These results imply a strong seasonal modulation of the accuracy of geostrophic velocity diagnosed from submesoscale sea-surface height delivered by the Surface Water and Ocean Topography (SWOT) satellite mission.

1. Introduction

Recent interest in upper-ocean dynamics has focused on the strong seasonal cycle of shallow baroclinic instabilities and their role in submesoscale (roughly 1-100 km) turbulence and mesoscale (roughly 100-300 km) modulation [Sasaki *et al.*, 2014; Qiu *et al.*, 2014; Brannigan *et al.*, 2015; Callies *et al.*, 2015; Thompson *et al.*, 2016; Buckingham *et al.*, 2016]. Contemporary studies have also shown that inertia-gravity waves (IGWs) contribute significantly to the near-surface variability at submesoscales [Richman *et al.*, 2012; Böhler *et al.*, 2014; Rocha *et al.*, 2016], but their seasonality has not been investigated.

The partition between geostrophic and ageostrophic flows across the submesoscales and their seasonality have immediate applications for the planning of the Surface Water and Ocean Topography (SWOT) satellite mission. SWOT will deliver sea-surface height (SSH) with about 15 km resolution, thereby providing the first global SSH measurements at submesoscales [Fu and Ubelmann, 2014]. Thus, the projection of energetic submesoscale ageostrophic flows, such as inertia-gravity waves (IGWs), onto SSH represents a challenge and an opportunity for the SWOT community. The challenge: how to diagnose submesoscale surface velocity from SSH. The opportunity: stimulation of research on interactions between geostrophic and ageostrophic flows and their projection onto SSH.

Using the output of two comprehensive global numerical simulations, here we show that IGWs undergo a strong near-

surface seasonal cycle in the Kuroshio Extension region. Interestingly, the seasonal cycle of IGWs is out of phase with the seasonal cycle of submesoscale turbulence. Consistent with previous studies, submesoscale turbulence is strongest in winter [Sasaki *et al.*, 2014; Qiu *et al.*, 2014].

IGWs with horizontal scales between 10-100 km (hereafter submesoscale IGWs), however, peak in late summer/early fall, when the upper ocean is strongly stratified. Thus there exists a strong seasonal modulation of upper-ocean submesoscale dynamics: submesoscale turbulence dominates the upper-ocean dynamics in late winter/early fall, whereas submesoscale IGWs prevail in late summer/early fall.

2. The LLC numerical simulations

We use results of two latitude-longitude polar cap (LLC) comprehensive numerical simulations. The outputs analyzed here, LLC2160 (nominal resolution $1/24^\circ \approx 4.7$ km; effective resolution ≈ 20 km) and LLC4320 (nominal resolution $1/48^\circ \approx 2.3$ km; effective resolution ≈ 8 km), are forward solutions of the Massachusetts Institute of Technology general circulation model [MITgcm; Marshall *et al.*, 1997] on a LLC grid [Forget *et al.*, 2015] with 90 vertical levels. The coarser-resolution LLC simulation was spun up from an Estimating the Circulation and Climate of the Ocean, Phase II [ECCO2; Menemenlis *et al.*, 2008] adjoint-method state estimate, constrained to millions of observations from 2009 through 2011.

The LLC2160 output spans two years from March 2011 to April 2013; the LLC4320 was spun up from the LLC2160 simulation, spanning one year from September 2011 to October 2012. Both LLC2160 and LLC4320 simulations were forced by tides hourly and by 6-hourly surface atmospheric fields. The LLC4320 simulation is an extension of the 3-month long output used by Rocha *et al.* [2016] — for details, see supporting information.

Tidal forcing by the 16 most-significant components represents a key feature of the LLC2160 and LLC4320 simulations. Barotropic tides flowing over topography convert significant tidal energy into the internal wave field. Those internal waves project onto mesoscales to submesoscales [e.g., Rocha *et al.*, 2016]. Hence tidal forcing fundamentally distinguishes our analysis from other modeling studies of seasonality [Sasaki *et al.*, 2014; Qiu *et al.*, 2014].

¹Scripps Institution of Oceanography, University of California San Diego, La Jolla, CA, USA.

²Earth Sciences Division, Jet Propulsion Laboratory, California Institute of Technology, Pasadena, CA, USA.

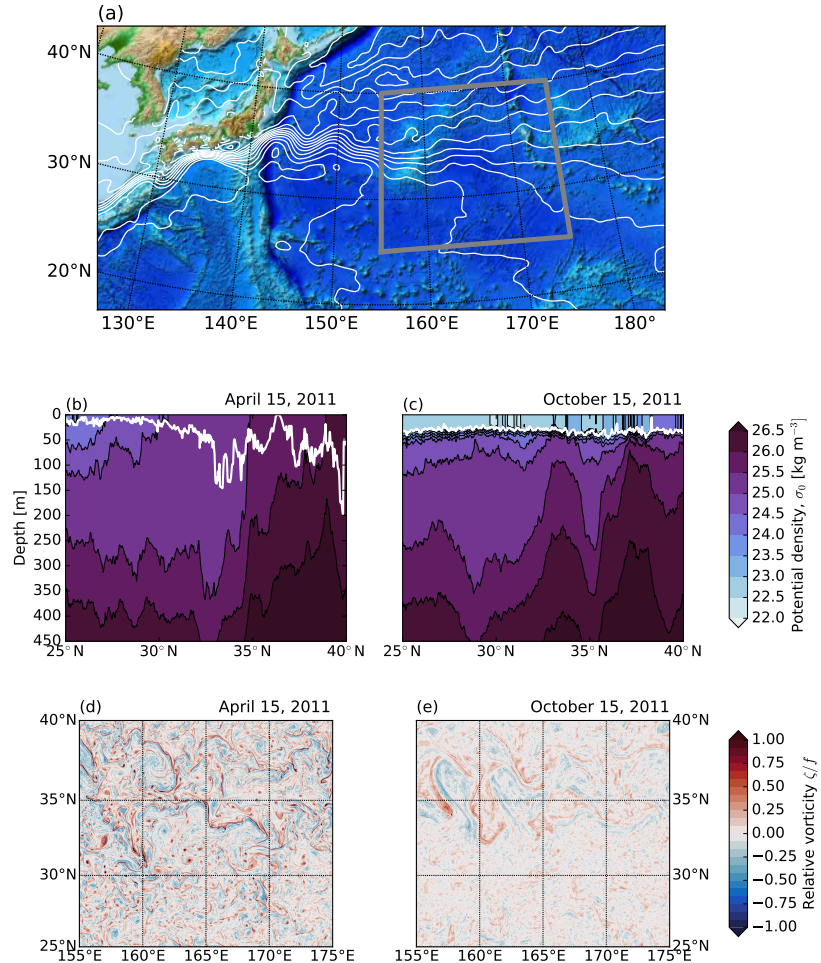


Figure 1. (a) The study region with the subregion where the LLC outputs are analyzed. Colors represent the topography and white lines are contours of absolute dynamic topography every 0.1 m from AVISO. LLC 4320 (1/48°) snapshots of transects of potential density at 165°E (b and c) and surface vorticity (d and e). In (b) and (c) the white line represents the mixed layer depth. The snapshots were taken at 12:00 UTC.

To study seasonal variations in the upper-ocean dynamics, we focus on the northwest Pacific, in the vicinity of the Kuroshio Extension, where previous studies have shown strong mesoscale and submesoscale seasonality [Sasaki *et al.*, 2014; Qiu *et al.*, 2014]. We analyze a sub-domain of the LLC4320 and LLC2160 simulations of about 2000 km² spanning 155–175°E; 25–40°N (Figure 1a). The stratification in this mesoscale-rich subtropical region undergoes a vigorous seasonal cycle: wintertime-enhanced small-scale turbulence de-stratifies the upper ocean, yielding mixed layers deeper than 200 m to the north (Figure 1b). Summertime re-

stratification yields mixed layers shallower than 40 m (Figure 1c).

Fundamentally, the upper-ocean density structure is well-captured by both LLC simulations: a comparison with Argo climatology [updated from Roemmich and Gilson, 2009] shows that both simulations skillfully represent the Kuroshio Extension stratification and its seasonal variability (supporting information). Moreover, model smoothed fields have eddy kinetic energy (EKE) levels (0.041 m² s⁻²) similar to Jason II across-track geostrophic EKE (0.036 m² s⁻²) and gridded geostrophic EKE (0.032 m² s⁻²).

3. Bulk statistics of the surface lateral velocity gradient tensor

To study the seasonality in the surface velocity, we calculate the lateral velocity gradient tensor

$$\begin{bmatrix} u_x & u_y \\ v_x & v_y \end{bmatrix} \quad (1)$$

using a centered second-order finite difference scheme — we obtain qualitatively similar results using spectral differentiation of velocity fields periodized with reflections; statistics of fields obtained via spectral differentiation are 10-15% larger. We then diagnose the vertical vorticity

$$\zeta \equiv v_x - u_y, \quad (2)$$

lateral rate of strain

$$\alpha \equiv [(u_x - v_y)^2 + (u_y + v_x)^2]^{1/2}, \quad (3)$$

and horizontal divergence

$$\delta \equiv u_x + v_y. \quad (4)$$

Because vortices, fronts, and IGWs are ubiquitous at submesoscales, second-order statistics of vorticity, strain, and divergence highlight these fine lateral scales [e.g., *Shcherbina et al.*, 2013].

The model solutions depict seasonality in vorticity (Figures 1d-e): large values of fine-grained vertical vorticity are observed in early spring with maximum values as large as $4f$, where f is the local planetary vorticity, and root-mean-square (RMS) of about $0.4f$. In early fall, the situation is the opposite: the vertical vorticity is relatively coarse-grained; its local maximum and RMS are both smaller than $0.5f$. Indeed, the vorticity and rate of strain are strongest in wintertime (Figure 2): in both simulations, the RMS vorticity and strain rate are about twice as large in late winter/early spring than in late summer/early fall. Because the wintertime vorticity and strain rate are dominated by the smallest scales in the flow (the KE spectrum is shallower than a -3 power law in winter), increasing the resolution from $1/24^\circ$ to $1/48^\circ$ increases the wintertime RMS vorticity and strain by about 40%.

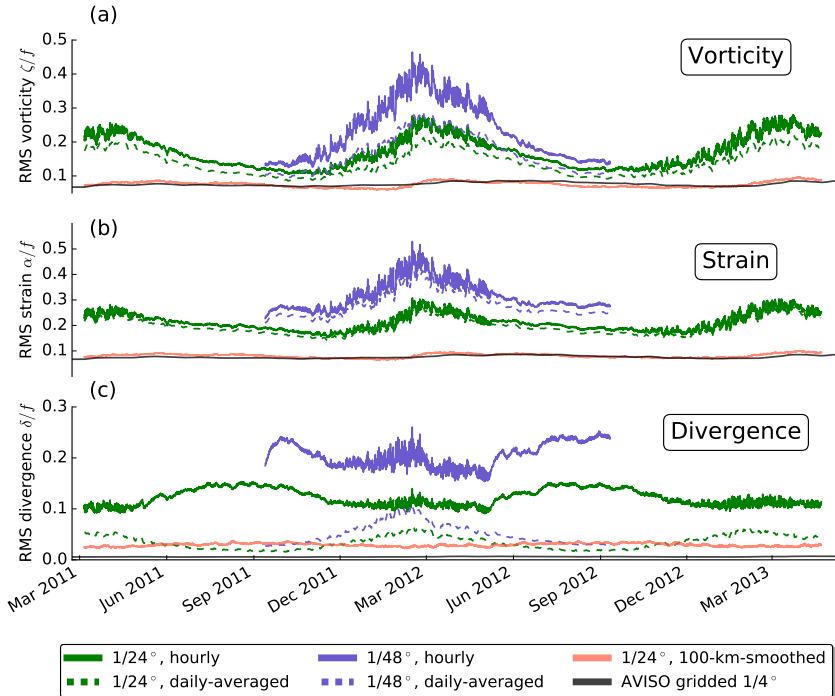


Figure 2. Time series of the root-mean-square (RMS) of surface (a) vorticity, (b) rate of strain, and (c) horizontal divergence in the LLC outputs and gridded AVISO data. The convergence of meridians account for the small RMS divergence in AVISO line in (c).

Subinertial flows account for the bulk of vertical vorticity and strain rate ($T_{32.5} = 2\pi/f_{32.5} \approx 22.3$ h, where $f_{32.5}$ is the inertial frequency at the mid-latitude 32.5°N): daily-averaging the velocity fields suppresses super-inertial motions and reduces the RMS vorticity by 40% and the RMS strain by 10%; the seasonal cycle remains strong (see dashed lines in figures 2a-b). Indeed, submesoscale flows account for most of this seasonal cycle: smoothing the velocity fields with a Hanning filter with cut off scale of 100 km dramatically reduces the RMS vorticity and strain rate. The reduction in variance is about 80% in winter, yielding RMS vorticity and strain rate roughly consistent with the diagnostics from AVISO gridded geostrophic velocities (compare red lines to black lines in figures 2a-b). The picture that emerges is consistent with recent studies: shallow baroclinic instabilities energize the submesoscales in winter, drawing from the available potential energy stored in large lateral buoyancy gradients in deep mixed layers [Sasaki et al., 2014; Callies et al., 2015, 2016].

The seasonal cycle of the horizontal divergence, however, showcases the complexity of the upper-ocean annual variability. If submesoscale turbulence dominated the near-surface variability all year, then the seasonal cycle of horizontal divergence, vertical vorticity, and lateral strain rate would be in phase [e.g., Sasaki et al., 2014]. While there is a clear wintertime peak in divergence of daily-averaged velocity (see dashed lines in figure 2c; RMS divergence $\sim 0.1f$ in the $1/48^\circ$ simulation), the hourly fields show a stronger enhancement of lateral divergence in late summer/early fall (RMS divergence $\sim 0.22f$ in the $1/48^\circ$ simulation). Because the $1/48^\circ$ simulation better resolves smaller-scale submesoscale flows, a secondary RMS divergence peak in winter is nearly as strong as in summer. Submesoscale fronts and eddies evolve relatively fast, and there is no clear temporal and spatial scale separation between those motions and IGWs [McWilliams, 2016]: daily-averaging the velocity fields efficiently suppresses the summertime horizontally divergent flows, but also reduces the wintertime lateral divergence by about 50%. Figure 2c also shows that most of the lateral diver-

gence is associated with submesoscale flows: smoothing

the velocity fields with a 100-km-cutoff suppresses more than 80% of the RMS divergence.

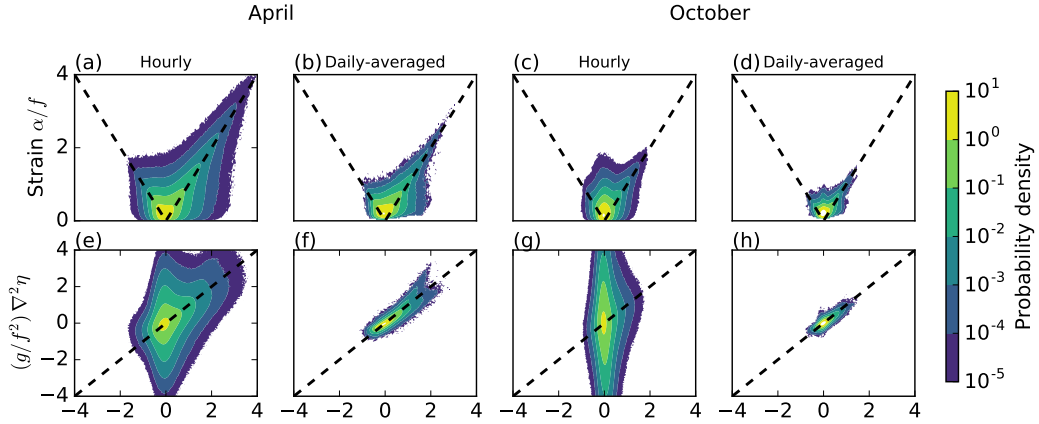


Figure 3. Seasonal variation of joint probability distributions of surface lateral velocity gradient tensor: vorticity vs. strain rate (a through d), and vorticity vs. Laplacian of sea-surface height (e through h) in April (a, b, e, f) and October (c, d, g, h). Dashed lines in (a) through (d) represent one dimensional shear flow $\alpha = \pm\zeta$, characteristic of fronts. Dashed lines in (e) through (h) represent geostrophic flow $\zeta = \frac{g}{f^2} \nabla^2 \eta$.

4. Joint probability density functions

The results of figure 2a-c show that submesoscale surface variability stems from different dynamics in summer than in winter. To characterize these differences, we calculate joint probability distributions (joint-PDF) of vorticity-strain and vorticity-Laplacian of sea-surface height (Figure 3).

The April vorticity-strain joint-PDF has a shape characteristic of submesoscale turbulence (Figures 3a-b). The alignment of vorticity and strain $\alpha \sim \pm\zeta$ with strong positive skewness are fingerprints of submesoscale fronts [Shcherbina et al., 2013; McWilliams, 2016]. The shape of the vorticity-strain joint-PDF is similar for hourly and daily-averaged fields, although the vorticity skewness reduces from 1.4 to 1.13 from hourly to daily-averaged. The April results indicate that wintertime submesoscale surface velocity is strongly dominated by submesoscale turbulence. The daily-averaged fields are largely in geostrophic balance, but the hourly velocity and sea-surface height fields have an important ageostrophic component as depicted by the joint-PDF of vorticity-Laplacian of SSH winter (Figure 3e).

The October vorticity-strain joint-PDF shows much weaker skewness (the vorticity skewness is 0.68 and 0.67 for hourly and daily-averaged velocities). The shape of the vorticity-strain joint-PDF appears to be a combina-

tion of two half-ellipses centered about $\zeta = 0$, one with a 45° slope (characteristic of submesoscale fronts that persist in summer) and one with a very steep slope. That the submesoscale dynamics in October are mainly ageostrophic is clearly depicted in the shape of joint-PDF of vorticity-Laplacian of sea-surface height for hourly fields (Figure 3g), which is an ellipse aligned in the vertical axis. Daily-averaging the model suppresses the ageostrophic, super-inertial flows, and, therefore, the daily-averaged flow is essentially geostrophic as depicted by the 45°-tilted ellipse in the vorticity-Laplacian of sea-surface height joint-PDF (Figure 3h).

Time series of PDFs of vorticity and divergence (supporting information) show a strong oscillation between these two regimes. In late winter/early spring the vorticity is strongly positively skewed, whereas the divergence is moderately negatively skewed (convergence/downwelling) as predicted by frontogenesis [e.g., McWilliams, 2016]. In late summer/early fall, the divergence is stronger, but PDFs are much less skewed, consistent with a superposition of random linear IGWs [e.g., Garrett and Munk, 1972].

5. Wavenumber-frequency spectrum

To confirm that submesoscale IGWs account for most of the super-inertial SSH variance and surface KE, we

calculate the wavenumber-frequency spectrum of SSH variance. Focusing on the high-frequency content, we compute the wavenumber-frequency spectrum every 10 days and average the results to obtain a spectral es-

timate. Before calculating the discrete Fourier transform, we remove linear trends and multiply the data by a three-dimensional Hanning window. We azimuthally-average the spectrum in wavenumber.

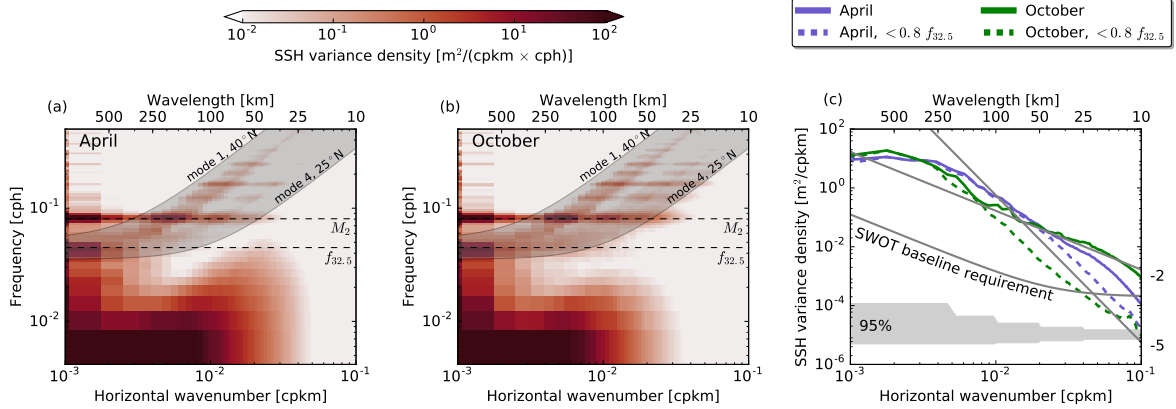


Figure 4. LLC4320 wavenumber-frequency spectrum of SSH variance in (a) April and (b) October. (c) Wavenumber spectrum of SSH variance — the integral of (a) and (b) over frequency. In (a) and (b), the light gray shaded region depicts the dispersion relations for inertia-gravity waves from mode 1 through mode 4 across the latitudinal domain; horizontal dashed lines represent the semi-diurnal lunar tidal frequency (M_2) and the inertial frequency at mid-latitudes ($f_{32.5}$). For reference, the gray line shows the baseline requirement as specified by the SWOT science team [Rodriguez, 2014].

Mesoscales flows and the lunar semi-diurnal tide contain most of the SSH variance (Figures 4a-b). But there is significant SSH variance at submesoscales, both sub-inertial and super-inertial. Sub-inertial SSH variance at submesoscales is larger in April, whereas super-inertial SSH variance at submesoscales is larger in October. At scales smaller than 100 km (submesoscales), the SSH variance is 66% larger in October than in April. IGWs, particularly modes two through four, account for most of the SSH variance increase in summer — higher vertical modes are more sensitive to changes in near-surface stratification (supporting information). In October, super-inertial IGWs account for a SSH standard deviation of about 4.9 cm, comparable to the April sub-inertial SSH standard deviation of ~5.2 cm (Table 1). Similarly, the submesoscale super-inertial surface

KE is 63% larger in October than in April (supporting information).

Figure 4c shows the integral over frequency of wavenumber-frequency spectra in figures 4a-b. Both in April and October, the SSH wavenumber spectrum approximately follows a -2 power-law at submesoscales (solid lines in figure 4c) — there is small difference between the spectra owing to the phase cancellation between the seasonal cycle of submesoscale turbulence and IGWs. The sub-inertial flow has a steeper submesoscale SSH variance wavenumber spectrum (dashed lines in figure 4c). The difference between the SSH variance wavenumber spectrum for all frequencies and sub-inertial frequencies is dramatic in October when super-inertial flows account for about 80% of the SSH variance and KE at submesoscales — we obtain similar results by computing SSH variance and KE wavenumber spectra directly from hourly and daily-averaged SSH velocity fields.

6. Discussion and conclusion

Our work adds to recent model [e.g., Sasaki *et al.*, 2014] and observational [e.g., Callies *et al.*, 2015; Buckingham *et al.*, 2016] evidence of vigorous seasonality in submesoscale turbulence. In particular — in global simulations with embedded tides — near-surface sub-

Table 1. The square root of the mean-square SSH at submesoscales (10-100 km) estimated from the wavenumber-frequency spectrum of SSH variance in figure 4. The SWOT baseline requirement at 15 km is approximately $\sqrt{2}$ cm.

| | April | October |
|--------------------------------|--------|---------|
| sub-inertial (< 0.8f) | 5.2 cm | 2.0 cm |
| super-inertial (> 1.2f) | 2.9 cm | 4.9 cm |
| near-f (0.8 – 1.2f) | 0.3 cm | 0.4 cm |
| near- M_2 (0.8 – 1.2 M_2) | 1.5 cm | 3.1 cm |

mesoscale IGWs undergo a strong seasonal cycle that is out of phase with the seasonal cycle of submesoscale turbulence. IGW energy and SSH variance are significantly spread across the submesoscales, likely through mesoscale advection and refraction, and dispersion [e.g., *Ponte and Klein, 2015; Alford et al., 2016*, and references therein] and parametric sub-harmonic instability [PSI, e.g., *MacKinnon and Winters, 2005*], though the LLC simulations are unlikely to fully resolve PSI. In the LLC simulations, super-inertial IGWs account for most of the surface submesoscale KE and SSH variance; near-inertial IGWs project onto larger scales, possibly because submesoscale NIWs quickly propagate into the interior and weakly project onto SSH.

D'Asaro [1978] showed that the velocity of linear internal waves in the mixed layer strongly depends on the density jump at the mixed layer base, with largest velocities when the jump is strongest. In summer, the shallow mixed layer overlays a strong seasonal pycnocline, and thus the internal waves projection onto the mixed layer may be stronger according to *D'Asaro [1978]*'s arguments. An alternative explanation is that the shape of the baroclinic modes changes seasonally [see *World Ocean Atlas 2013, Levitus et al., 2013*, modal shapes in the supporting information].

Internal tide energy flux does not show a seasonal modulation [e.g., *Alford, 2003*]; hence one expects a strong seasonality in the near-surface expression of internal tides and higher frequency IGWs if the near-surface stratification varies strongly. The intermittent windy near-inertial wave (NIW) generation peaks in early winter, but NIW energy has a similar energy level in October and April [*Alford et al., 2016*]. Furthermore, in our simulations the higher frequency inertia-gravity waves account for most of the seasonality in super-inertial surface KE and SSH (Figure 4a-b).

The seasonally varying mixed-layer depth challenges observation and simulation of flows at mixed-layer deformation-radius length scale in observational programs and models with fixed resolution [*Buckingham et al., 2016*]. But the mixed layer available potential energy is lowest in summer owing to shallow mixed-layer depths and weak lateral buoyancy gradients [*Callies et al., 2015*]. Moreover, in baroclinic turbulence, the deformation radius has only a secondary, catalytic role — most of the baroclinic conversion occurs at larger scales [*Larichev and Held, 1995; Callies et al., 2016*]. Thus, the model failure to resolve the summertime ML deformation radius is unlikely to account for the vigorous seasonality in submesoscale turbulence.

In the context of SWOT, these results imply that if one is interested only in the geostrophic flow, so that surface velocity can be diagnosed from SSH, then the noise-to-signal ratio will have a strong seasonality owing to the presence of IGWs (the coherent fraction of internal tides may be removed efficiently). An important caveat is that the Kuroshio Extension may be typ-

ical of a mesoscale-rich subtropical regions, but it is unlikely to be representative of other regions such as low-eddy-kinetic-energy eastern boundary currents. We plan to report on the geographic variability of submesoscale seasonality in a future study.

Acknowledgments. William R. Young and three reviewers provided helpful and stimulating comments. Greg Wagner suggested that the near-surface shape of the baroclinic modes changes seasonally. We thank the MITgcm community and our colleagues at the NASA Advanced Supercomputing (NAS) Division for their awesome support. This research was funded by NSF (OCE1357047) and NASA (NNX13AE44G, NNX13AE85G, NNX16AH67G, NNX16AO5OH). The LLC output can be obtained from the ECCO project (http://ecc2.org/l1c_hires). The altimeter products were produced by Ssalto/Duacs and distributed by AVISO, with support from CNES (<http://www.aviso.altimetry.fr/duacs/>). Codes and output files are available online at the project repository (<https://github.com/crocha700/UpperOceanSeasonality>).

References

- Alford, M. H. (2003), Redistribution of energy available for ocean mixing by long-range propagation of internal wave, *Nature*, **423**(6936), 159–162.
- Alford, M. H., J. A. MacKinnon, H. L. Simmons, and J. D. Nash (2016), Near-inertial internal gravity waves in the ocean, *Annual review of marine science*, **8**, 95–123.
- Brannigan, L., D. P. Marshall, A. Naveira-Garabato, and A. G. Nurser (2015), The seasonal cycle of submesoscale flows, *Ocean Modelling*, **92**, 69–84.
- Buckingham, C. E., A. C. Naveira Garabato, A. F. Thompson, L. Brannigan, A. Lazar, D. P. Marshall, A. George Nurser, G. Damerell, K. J. Heywood, and S. E. Belcher (2016), Seasonality of submesoscale flows in the ocean surface boundary layer, *Geophysical Research Letters*, **43**(5), 2118–2126.
- Bühler, O., J. Callies, and R. Ferrari (2014), Wave-vortex decomposition of one-dimensional ship-track data, *Journal of Fluid Mechanics*, **756**, 1007–1026.
- Callies, J., R. Ferrari, J. M. Klymak, and J. Gula (2015), Seasonality in submesoscale turbulence, *Nature communications*, **6**.
- Callies, J., G. Flierl, R. Ferrari, and B. Fox-Kemper (2016), The role of mixed-layer instabilities in submesoscale turbulence, *Journal of Fluid Mechanics*, **788**, 5–41.
- D'Asaro, E. A. (1978), Mixed layer velocities induced by internal wave, *Journal of Geophysical Research: Oceans*, **83**(C5), 2437–2438.
- Forget, G., J.-M. Campin, P. Heimbach, C. Hill, R. Ponte, and C. Wunsch (2015), ECCO version 4: an integrated framework for non-linear inverse modeling and global ocean state estimation, *Geosci. Model Dev.*, **8**, 3071–3104.
- Fu, L.-L., and C. Ubelmann (2014), On the transition from profile altimeter to swath altimeter for observing global ocean surface topography, *Journal of Atmospheric and Oceanic Technology*, **31**(2), 560–568.
- Garrett, C., and W. Munk (1972), Space-time scales of internal waves, *Geophysical & Astrophysical Fluid Dynamics*, **3**(1), 225–264.
- Larichev, V. D., and I. M. Held (1995), Eddy amplitudes and fluxes in a homogeneous model of fully developed baroclinic instability, *Journal of physical oceanography*, **25**(10), 2285–2297.
- Levitus, S., J. Antonov, O. K. Baranova, T. Boyer, C. Coleman, H. Garcia, A. Grodsky, D. Johnson, R. Locarnini, A. V. Mishonov, et al. (2013), The world ocean database, *Data Science Journal*, **12**(0), WDS229–WDS234.
- MacKinnon, J., and K. Winters (2005), Subtropical catastrophe: Significant loss of low-mode tidal energy at 28.9, *Geophysical Research Letters*, **32**(15).
- Marshall, J., C. Hill, L. Perelman, and A. Adcroft (1997), Hydrostatic, quasi-hydrostatic, and nonhydrostatic ocean modeling, *Journal of Geophysical Research: Oceans*, **102**(C3), 5733–5752.

- McWilliams, J. C. (2016), Submesoscale currents in the ocean, in *Proc. R. Soc. A*, vol. 472, p. 20160117, The Royal Society.
- Menemenlis, D., J.-M. Campin, P. Heimbach, C. Hill, T. Lee, A. Nguyen, M. Schodlok, and H. Zhang (2008), ECCO2: High resolution global ocean and sea ice data synthesis, *Mercator Ocean Quarterly Newsletter*, 31, 13–21.
- Ponte, A. L., and P. Klein (2015), Incoherent signature of internal tides on sea level in idealized numerical simulations, *Geophysical Research Letters*, 42(5), 1520–1526.
- Qiu, B., S. Chen, P. Klein, H. Sasaki, and Y. Sasai (2014), Seasonal mesoscale and submesoscale eddy variability along the North Pacific Subtropical Counter-current, *Journal of Physical Oceanography*, 44(12), 3079–3098.
- Richman, J. G., B. K. Arbic, J. F. Shriver, E. J. Metzger, and A. J. Wallcraft (2012), Inferring dynamics from the wavenumber spectra of an eddying global ocean model with embedded tides, *Journal of Geophysical Research: Oceans*, 117(C12).
- Rocha, C. B., T. K. Chereskin, S. T. Gille, and D. Menemenlis (2016), Mesoscale to submesoscale wavenumber spectra in Drake Passage, *Journal of Physical Oceanography*, 46, 601–620.
- Rodriguez, E. (2014), Surface Water and Ocean Topography Mission (SWOT): Science Requirements Document.
- Roemmich, D., and J. Gilson (2009), The 2004–2008 mean and annual cycle of temperature, salinity, and steric height in the global ocean from the Argo Program, *Progress in Oceanography*, 82(2), 81–100.
- Sasaki, H., P. Klein, B. Qiu, and Y. Sasai (2014), Impact of oceanic-scale interactions on the seasonal modulation of ocean dynamics by the atmosphere, *Nature communications*, 5.
- Shcherbina, A. Y., E. A. D'Asaro, C. M. Lee, J. M. Klymak, M. J. Molemaker, and J. C. McWilliams (2013), Statistics of vertical vorticity, divergence, and strain in a developed submesoscale turbulence field, *Geophysical Research Letters*, 40(17), 4706–4711.
- Thompson, A. F., A. Lazar, C. Buckingham, A. C. Naveira Garabato, G. M. Damerell, and K. J. Heywood (2016), Open-ocean submesoscale motions: A full seasonal cycle of mixed layer instabilities from gliders, *Journal of Physical Oceanography*, 46(4), 1285–1307.

Corresponding author: Cesar B. Rocha, Scripps Institution of Oceanography, University of California San Diego, La Jolla, CA, USA. (crocha@ucsd.edu)